A&A, 706, L4 (2026)
https://doi.org/10.1051/0004-6361/202557939

Astronomy & Astrophysics

LETTER TO THE EDITOR

Identification of solid N_2O in interstellar ices using open JWST data

V. Karteyeva*, R. Nakibov, I. Petrashkevich, M. Medvedev, and A. Vasyunin

Research Laboratory for Astrochemistry, Ural Federal University, Kuibysheva St. 48, Yekaterinburg 620026, Russia

Received 2 November 2025 / Accepted 3 January 2026

ABSTRACT

Context. Only six molecules containing an N-O bond are detected in the gaseous phase of the interstellar medium. One of them is nitrous oxide (N_2O), which was unsuccessfully searched for in solid form since the launch of the Infrared Space Observatory (ISO) mission. The observational capabilities of the *James Webb* Space Telescope (JWST) present the possibility of identifying solid interstellar N_2O.

Aims. We aim to identify nitrous oxide in open JWST spectra of interstellar ices toward a sample of Class 0, 0/I, and flat protostars using the relevant laboratory mixtures of N_2O-bearing interstellar ice analogs.

Methods. A set of laboratory infrared transmission spectra was obtained for the following mixtures: N_2O:CO_2 = 1:20, N_2O:CO = 1:20, N_2O:N_2 = 1:20, N_2O:CO_2:CO = 1:15:5, and N_2O:CO_2:N_2 = 1:15:13 at 10–23 K. A search for N_2O in JWST NIRSpec spectra toward 50 protostars was performed by fitting the 4.44–4.47 μm (2250–2235 cm^{-1}) NN-stretch absorption band with new laboratory mixtures of N_2O-bearing ices.

Results. We claim the first secure identification of N_2O in 16 protostars. The fitting results show that N_2O is formed predominantly within the apolar layer of the ice mantles, which are rich in CO, CO_2, and N_2. The abundance of solid N_2O is estimated at 0.2–2.1% relative to solid CO. We present the band strengths for N_2O in the mixtures corresponding to the apolar layer. We also report the identification of the C-N stretch band at 4.42 μm (2260 cm^{-1}), which we tentatively assign to HNCO, the simplest C-N bond carrier.

Key words. astrochemistry – molecular data – methods: laboratory: molecular – stars: protostars – ISM: abundances – ISM: molecules

1. Introduction

Nitrous oxide (N_2O) is one of the six N–O bond molecules that are detected in the gaseous phase (McGuire 2022). They are important for the evolution of the molecular complexity in space. While it was detected in the gaseous phase in various astronomical environments, namely, in the Sgr B2 interstellar cloud (Ziurys et al. 1994; Halfen et al. 2001), in the protostellar binary IRAS 16293-2422 (Ligterink et al. 2018), in the G+0.693 molecular cloud (Rivilla et al. 2020), and in the atmosphere of Mars (Villanueva et al. 2013), its solid-state counterpart, which might be a tracer of nitrogen chemistry in icy grain mantles, remains elusive. The detection of solid N_2O may serve as a tracer in the formation of more complex nitrogen-bearing molecules (Fedoseev et al. 2018) and might act as a proxy for the presence and chemical activity of infrared-inactive molecules (N_2 and O_2) in ices (e.g. Elsila et al. 1997; Jamieson et al. 2005; Pereira et al. 2018). Nitrous oxide might provide a direct abiotic route to species of prebiotic relevance (Jamieson et al. 2005), and it was itself recently proposed as a potential biosignature (Schwieterman et al. 2022).

The search for solid N_2O in interstellar ices has been conducted for decades. Initial investigations with the Infrared Space Observatory (ISO) yielded negative results (Ehrenfreund et al. 1997), which highlights that it is hard to identify. Laboratory studies, however, showed that N_2O may be produced by UV irradiation of apolar ices (Elsila et al. 1997; Moore & Hudson 2003). More recent experimental works also suggested that N_2O might be a component of cold interstellar ices and might form efficiently through ion bombardment (e.g. Jamieson et al. 2005; Sicilia et al. 2012; Pereira et al. 2018) of apolar N_2-containing ices. This makes it a promising candidate for future observations.

N_2O can also be formed after ion bombardment of nitrous oxides, as shown in experiments with NO_2:N_2O_4 mixture at 16 K and 60 K (Fulvio et al. 2019). Finally, modeling predicts N_2O to be the most abundant of the nitrous oxides (N_xO_y) that form under the ion bombardment of N_2-containing ices (Queiroz et al. 2025).

The unprecedented quality of the *James Webb* Space Telescope (JWST) data reignited the search for N_2O. Recent studies reported tentative detections in the 4.4–4.52 μm (2272–2212 cm^{-1}) region (Nazari et al. 2024) based on the spectrum of pure crystalline N_2O at 70 K and in the 7.7 μm band toward the Ced 110 IRS4A protostar, where a spectrum of pure irradiated N_2O was used (Rocha et al. 2025). This provided the first N_2O column density estimate: 8.1×10^{16} cm^{-2} (1.8% relative to solid H_2O). The analysis of IRAS 23385+6053 also suggested a tentative assignment of a feature in the 7.7 μm region to N_2O (Nakibov et al. 2025) based on underfitting in this region.

However, using the laboratory spectra of pure or irradiated N_2O is unreliable because interstellar ices have complex chemical composition. N_2O is expected to be a trace component that is likely embedded in CO/CO_2-rich (apolar) environments. Moreover, the infrared-band profiles and peak positions of solid species are known to shift significantly depending on the molecular environment. Currently, the following

* Corresponding author: varvara.karteeva@urfu.ru

N_2O infrared (IR) laboratory transmission spectra are available: pure N_2O in the range of 10–70 K (Hudson et al. 2017; Gerakines & Hudson 2020), pure N_2O at 16 K (Fulvio et al. 2009), N_2O:H_2O = 1:29 at 14 K (Bergantini et al. 2022), and N_2O:CO_2 = 1:2 at 11 K (Pereira et al. 2018). Because the high-quality observational JWST data are available the lack of relevant reference data becomes a primary obstacle to a secure identification. The feature in the range of 2250–2235 cm^{-1} in the open JWST data that we explored is a candidate for a solid interstellar N_2O assignment based on the NN stretching mode. This region likely contains the absorption band of the N_2O in the apolar environment (e.g. CO_2, CO, and N_2) because laboratory mixtures of N_2O in the polar layer do not match this range (see e.g. Bergantini et al. 2022). Several studies supported the origin of N_2O in apolar N_2-bearing ices: CO:N_2, N_2:O_2:CO, N_2:O_2:CO_2:CO (Elsila et al. 1997), CO:N_2 (Moore & Hudson 2003), N_2:CO_2 (Jamieson et al. 2005), CO:N_2 (Sicilia et al. 2012), and N_2:O_2 (Lo et al. 2018).

We present the first reliable identification of solid N_2O in interstellar ices. We achieved this by combining the unparalleled sensitivity and resolution of JWST with a dedicated laboratory study of N_2O in the apolar environment. Our survey of 50 protostars of variable classes and masses available in the Mikulski Archive for Space Telescopes[1] (MAST) database revealed clear spectroscopic signatures of N_2O in 16 sources, which allowed us to derive its column density and establish first observational constraints on its environment in interstellar ice.

2. Experimental setup and methods

The transmission laboratory spectra we used for N_2O identification were obtained using the Ice Spectroscopy Experimental Aggregate (ISEAge), a cryogenic ultra-high vacuum setup described in detail in Ozhiganov et al. (2024). Briefly, the ISEAge setup allows us to produce and study interstellar ice analogs. The base pressure in the chamber prior to experiments is 2×10^{-10} mbar, and the temperature of the Ge substrate can be set and held within 6.7–305 K range. The transmission laboratory IR spectra were obtained with the Thermo Scientific Nicolet iS50 FTIR spectrometer operated within a 4000–630 cm^{-1} (2.5–15.9 μm) range with 1 cm^{-1} resolution. The ices were deposited via the background deposition technique (Accolla et al. 2011; Fedoseev et al. 2015; Rachid et al. 2021, 2022; Kruczkiewicz et al. 2024; Satorre et al. 2025). The individual deposition rates were calibrated using Stanford Research Systems RGA200 quadruple mass spectrometer (QMS) in combination with IR spectroscopy via the calibration curves, which we obtained following Slavicinska et al. (2023).

The ices were grown on a Ge substrate cooled down to 10 ± 0.1 K. The N_2O deposition rate was calibrated using the band strength of 5.891×10^{-17} cm for the ν_3 mode at 10 K taken from Hudson et al. (2017). In all the experiments, pure N_2O was introduced into the main UHV chamber at the desired fixed deposition rate through the first leak valve. Simultaneously, second gas or a precalibrated gas mixture was introduced into the main chamber through the second independent leak valve. The QMS signal is continuously monitored during the depositions to ensure that the deposition rate was consistent with the calibration curve values. The compositions of the deposited ice mixtures were verified by examining the features in IR spectra. Co-depositions continued for 120 minutes, and the N_2O deposition rate was fixed at 2.95×10^{12} cm^{-2} s^{-1}. This resulted in a total N_2O column density of 2×10^{16} cm^{-2}. The ice was then warmed up at a rate of 0.5 K per minute. During the warm-up, the IR laboratory spectra were recorded every 45 seconds (averaging over 32 scans). We present the transmission laboratory spectra of N_2O absorption in the apolar environment at 10 K and 23 K for the first time: N_2O:CO_2 = 1:20, N_2O:CO = 1:20, N_2O:N_2 = 1:20, N_2O:CO_2:CO = 1:15:5, and N_2O:CO_2:N_2 = 1:15:13. The N_2O absorption bands were isolated via baseline correction for further use.

The compounds we used are N_2O (99.999%, BK-Grypp), CO (99.9999%, Ugra-PGS), CO_2 (99.9999%, Ugra-PGS), and N_2 (99.9999%, Ugra-PGS). Gaseous N_2O, CO, CO_2, and N_2 were introduced directly into the dosing lines from the commercially acquired gas bottles.

3. Observations and fitting procedure

We focused on detecting N_2O by its most prominent ν_3 absorption band at ~4.45 μm. The 7.77 μm band (ν_1) is about four times less intense and was not analyzed because the signal-to-noise ratio in this region was too low.

We surveyed the MAST database for protostars observed with JWST Near-Infrared Spectrometer (NIRSpec) and compiled an initial list of 50 sources (MAST DOI: 10.17909/tg2a-kv41). NIRspec uses G395M/G395H modes with the spectral resolution of ~1000 and ~2700, respectively, and covers the range of 2.87–5.27 μm. We used science data with the level 3 pipeline calibration (calibration pipeline described by Greenfield & Miller 2016; Bushouse et al. 2024; van Gelder et al. 2024). We manually examined each source and searched for the apertures with detectable N_2O features based on our laboratory reference spectra. The search was challenging because the gaseous CO emission lines overlap with the region of interest, and therefore, we classified the sources into three groups:

+ Sources in which we were able to identify an aperture with N_2O features that had none or weak overlap with CO emission.
+ Sources in which we were able to identify an aperture with N_2O features that overlapped the CO emission, but the emission could be masked without causing severe distortions to the spectrum.
– Sources in which we were not able to identify an aperture with N_2O features due to strong CO emission and/or a low signal-to-noise ratio.

The search yielded 16 sources (MAST DOI: 10.17909/sg05-m334) in which we selected the apertures with minimal distortions in the N_2O region with the aim of a secure detection claim. In four objects, we recovered the N_2O feature from gaseous CO lines. For these sources, we provide an additional aperture with a clear N_2O feature. The intensity maps and chosen apertures are presented in Appendix A. The aperture parameters are presented in Table C.1.

We then prepared the laboratory spectra for the fitting procedure by subtracting the continuum and converting them into the optical depth. If required, we masked the gaseous CO emission lines. The details are presented in Appendix B. In some of the laboratory spectra, the N_2O feature overlaps a feature in 2280–2250 cm^{-1} (4.39–4.44 μm) region that is commonly associated with the CN-stretch band, for instance, isocyanic acid (HNCO) and acetonitrile (CH_3CN). The CN-stretch region also contained a gaseous emission doublet (H_2, Nazari et al. 2024) that lies in the range of 2270–2265 cm^{-1}, which hindered the identification

[1] MAST database: https://mast.stsci.edu/portal/Mashup/Clients/Mast/Portal.html

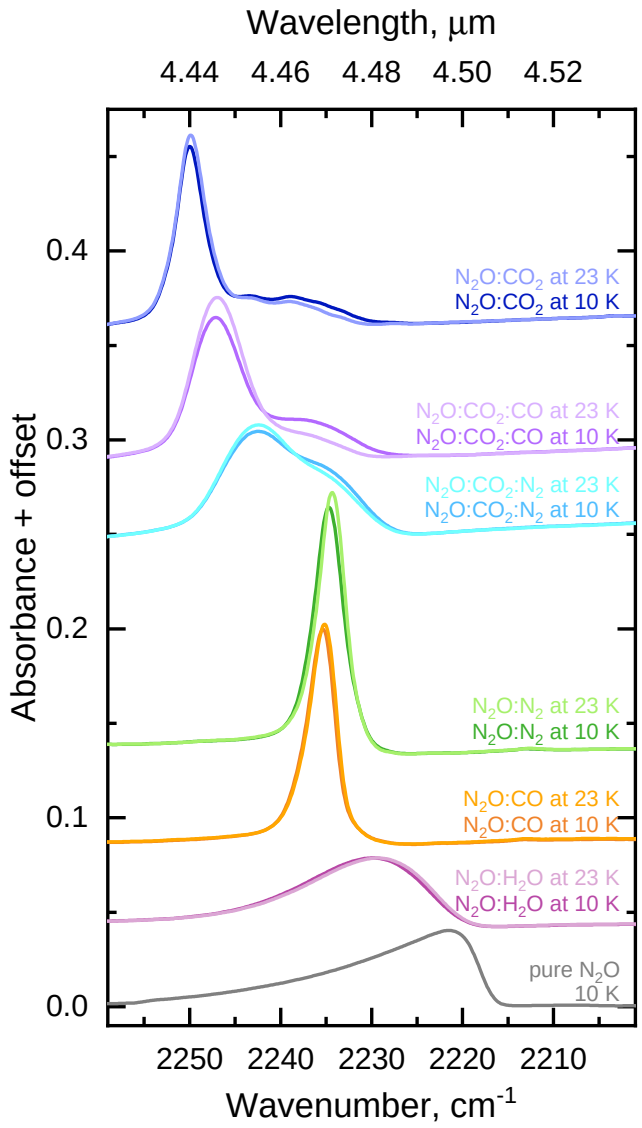

Fig. 1. ν_3 mode of N_2O in pure N_2O, N_2O:H_2O = 1:20 and nitrous oxide in astrochemically relevant matrices corresponding to the apolar layer of ice mantles N_2O:CO = 1:20, N_2O:N_2 = 1:20, N_2O:CO_2:N_2 = 1:15:13, N_2O:CO_2:CO = 1:15:5, and N_2O:CO_2 = 1:20. The spectra are displayed for the lowest and highest temperatures we considered.

of the exact carrier. We therefore tentatively assigned it to HNCO because it is the simplest CN-bearing molecule in this spectral region. A Gaussian function was included in the fit to cover the 2280–2250 cm^{-1} feature, which resolved the overlapped bands. We also fit Gaussian functions to estimate the column densities of CO, $^{13}CO_2$, and OCN^-. The $^{12}CO_2$ absorption band was not analyzed because it was saturated in the observational data. We also note that the profile of the intense solid CO feature at 4.67 μm toward protostars can be affected by grain shape effects (see, e.g. Pontoppidan et al. 2003, and references therein). This issue is not explored in this Letter, however.

The fitting was performed in two stages. For the first stage, we used the laboratory spectra of N_2O in the apolar environment: mixtures with CO, CO_2, and N_2 (see Fig. 1). The objects in our study are protostars, which are likely to have a temperature gradient in their inner regions. We, however, lack detailed constraints on the physical structure of these sources. The observational spectra show a strong solid CO absorption feature at 4.67 μm. The N-bearing ices we investigated also have relatively low sublimation temperatures. Finally, laboratory experiments proved the possibility of N_2O formation in N_2-containing ices at low temperatures (e.g., Fedoseev et al. 2018). We therefore assumed that the fitted spectral features originate from cold ices residing in cold protostar envelopes. Consequently, we use laboratory ice spectra obtained at temperatures below the sublimation point of N_2 (23 K) to analyze the observations. Each ice mixture spectrum is available at 35 discrete temperature points, spaced at even intervals of ~0.4 K. For each source, we performed a fit at each of these 35 temperatures T_i by modeling the observed spectral feature with a linear combination of laboratory spectra of different mixtures (all taken at that same T_i) plus an HNCO Gaussian function, minimizing χ^2,

$$\chi^2(T_i) = \sum_{j=1}^{N_{obs}} \frac{(\tau^j_{obs} - \tau^j_{lab}(T_i))^2}{\sigma^2_j}, \quad (1)$$

where τ_{obs} is the optical depth of the observational spectrum, and $\tau_{lab}(T_i)$ is the optical depth of a fitted linear combination of the laboratory spectra and the HNCO Gaussian at 2280–2250 cm^{-1}. T_i is the temperature of the fitted combination, N_{obs} is a number of points in the fitted segment of the observational spectrum, and σ_j is the point-wise standard deviation of the observational spectrum. A sliding-window smoothed curve (12–16 points, locally estimated weighted scatterplot smoothing, Cleveland 1979) was subtracted from the original optical depth spectrum to estimate σ_i from the residuals. From these 35 fits in the 10–23 K range, we then selected the overall best-fit spectrum for each source. Following Avni (1976), the error of the temperature estimates was obtained from the $\chi^2(T_i)$ line with $\Delta\chi^2 = 1$ ($\alpha = 68\%$). The column density errors were estimated as the best-fit uncertainty. The band strengths of N_2O in mixtures were estimated from band area measurements based on the value from Hudson et al. (2017, see the band strengths in our Table C.2).

In the second stage, the fitted spectrum was subtracted from the observational spectrum because the Gaussian in the 2280–2250 cm^{-1} region overlaps the $^{13}CO_2$ feature. Then, three Gaussian functions were fit to the residual spectrum to estimate the column densities of CO, OCN^- and $^{13}CO_2$. As in the first stage, the column density errors were estimated as the best-fit uncertainty.

4. Results and discussion

In Fig. 1 we present the new laboratory IR transmission spectra of N_2O-bearing mixtures in the apolar environment along with a pure N_2O and N_2O:H_2O mixture at 10 K and 23 K. The spectra obtained at intermediate temperatures are not shown because the shapes of the N_2O features vary smoothly in the 10–23 K range. The blueshift of the 4.45 μm (ν_3) feature with respect to its position in the spectrum of the pure N_2O is higher in the apolar environment than in N_2O:H_2O mixture. The highest blueshift of 28 cm^{-1} relative to pure N_2O is observed for the N_2O:CO_2 = 1:20 mixture. Ternary mixtures with CO_2 and CO/N_2 produce a broad N_2O feature that is limited by the peak positions observed for binary mixtures with CO_2 and CO/N_2 at a ratio of 1:20. The structure of the N_2O feature in ternary mixtures clearly indicates the presence of CO/N_2- and CO_2-associated components. This shows that the position and shape of the feature are sensitive to the ice composition. In summary, the N_2O absorption band in the apolar environment spans the

range of about 2250–2235 cm^{-1}, and its line shape depends on the composition.

In Fig. D.1 the observed spectra of N_2O-related feature for 20 apertures in 16 protostars are shown along with the best-fit results. The comparison with Fig. 1 shows that the spectral feature of the N_2O:H_2O mixture positioned at 2230 cm^{-1} falls outside the observed features. All derived temperatures and column densities are listed in Table C.1. In all observed sources, the JWST spectra were fit with the ice mixtures corresponding to the apolar layer of the ice mantles. The derived N_2O column densities relative to solid CO are in the range of 0.2–2.1%. Assuming a typical CO abundance relative to H_2O in a range of 10–30%, we estimated the N_2O abundance with respect to H_2O to be in the range of 0.02–0.84%. The 2280–2250 cm^{-1} band was tentatively assigned to the C-N stretch absorption band of HNCO. It is the simplest CN-stretch mode carrier, which commonly appears with N_2O in the irradiation experiments (see e.g. Fedoseev et al. 2018). Because of the H_2 emission in 2270–2265 cm^{-1} range, we constrained the HNCO peak position to 2260 ± 2 cm^{-1}, which agrees with the 2260 cm^{-1} HNCO feature reported by Fedoseev et al. (2018). We note that CH_3CN or C_2H_5CN are other possible candidates for this region (Nazari et al. 2024). The column densities obtained in this work for $^{13}CO_2$, OCN^- agree with values that were previously published in literature (see Appendix C for more details).

The detection of N_2O in the apolar layer agrees with the laboratory studies of the irradiation of N_2-bearing ices (e.g. Elsila et al. 1997; Lo et al. 2018). There are observational and chemical reasons for the nondetection of N_2O in the ~2230 cm^{-1} region, which corresponds to N_2O embedded in H_2O. In observational data for this region, the gaseous CO interference is stronger, which lowers the quality of the data and complicates the data selection. The chemical reason is the limited availability of N_2O key precursor, N_2, in H_2O-dominated ices (Hudson 2018). Interestingly, 8 of the 16 sources from the sample are the so-called HOPS sources in Orion A. Notably, this region is a subject to high UV background irradiation (Peeters et al. 2024), which further supports the irradiation-driven pathways of N_2O formation in interstellar ices.

Acknowledgements. This work is based on observations made with the NASA/ESA/CSA *James Webb* Space Telescope. The data were obtained from the Mikulski Archive for Space Telescopes at the Space Telescope Science Institute, which is operated by the Association of Universities for Research in Astronomy, Inc., under NASA contract NAS 5-03127 for JWST. We would like to thank Gleb Fedoseev and Vadim Krushinsky for assembling, calibrating and launching the ISEAge setup, and to Olga Russkikh for helpful discussions during manuscript revision. We thank the anonymous reviewer for their insightful comments that helped us to improve the manuscript and the language editor Astrid Peter for English corrections. This research work is funded by the Russian Science Foundation via 23-12-00315 agreement.

References

Accolla, M., Congiu, E., Dulieu, F., et al. 2011, PCCP, 13, 8037
Avni, Y. 1976, ApJ, 210, 642
Bergantini, A., de Barros, A. L. F., Toribio, N. N., et al. 2022, JPCA, 126, 2007
Bouilloud, M., Fray, N., Bénilan, Y., et al. 2015, MNRAS, 451, 2145
Brunken, N. G. C., van Dishoeck, E. F., Slavicinska, K., et al. 2024, A&A, 692, A163
Brunken, N. G. C., Boogert, A. C. A., van Dishoeck, E. F., et al. 2025, ESC, 9, 1992
Bushouse, H., Eisenhamer, J., Dencheva, N., et al. 2024, https://doi.org/10.5281/zenodo.10870758
Chen, H.-R. V., Keto, E., Zhang, Q., et al. 2016, ApJ, 823, 125
Cleveland, W. S. 1979, JASA, 74, 829
Ehrenfreund, P., d'Hendecourt, L., Dartois, E., et al. 1997, Icarus, 130, 1
Elsila, J., Allamandola, L. J., & Sandford, S. A. 1997, ApJ, 479, 818
Fedoseev, G., Ioppolo, S., Zhao, D., Lamberts, T., & Linnartz, H. 2015, MNRAS, 446, 439
Fedoseev, G., Scirè, C., Baratta, G. A., & Palumbo, M. E. 2018, MNRAS, 475, 1819
Fulvio, D., Sivaraman, B., Baratta, G. A., Palumbo, M. E., & Mason, N. J. 2009, AcSpA, 72, 1007
Fulvio, D., Baratta, G. A., Sivaraman, B., et al. 2019, MNRAS, 483, 381
Furlan, E., Fischer, W. J., Ali, B., et al. 2016, ApJS, 224, 5
Gerakines, P. A., & Hudson, R. L. 2020, ApJ, 901, 52
Gerakines, P. A., Materese, C. K., & Hudson, R. L. 2025, MNRAS, 537, 2918
Greenfield, P., & Miller, T. 2016, A&C, 16, 41
Halfen, D., Apponi, A., & Ziurys, L. 2001, ApJ, 561, 244
Hudson, R. L. 2018, ApJ, 867, 160
Hudson, R., Loeffler, M., & Gerakines, P. 2017, JChPh, 146, 024304
Jamieson, C. S., Bennett, C. J., Mebel, A. M., & Kaiser, R. I. 2005, ApJ, 624, 436
Kruczkiewicz, F., Dulieu, F., Ivlev, A. V., et al. 2024, A&A, 686, A236
Launhardt, R., Stutz, A. M., Schmiedeke, A., et al. 2013, A&A, 551, A98
Ligterink, N. F. W., Calcutt, H., Coutens, A., et al. 2018, A&A, 619, A28
Lo, J.-I., Chou, S.-L., Peng, Y.-C., et al. 2018, ApJ, 864, 95
McGuire, B. A. 2022, ApJS, 259, 30
Moore, M., & Hudson, R. 2003, Icarus, 161, 486
Nakibov, R., Karteyeva, V., Petrashkevich, I., et al. 2025, ApJ, 978, L46
Nazari, P., Rocha, W., Rubinstein, A., et al. 2024, A&A, 686, A71
Ortiz-León, G. N., Loinard, L., Dzib, S. A., et al. 2018, ApJ, 865, 73
Ozhiganov, M., Medvedev, M., Karteyeva, V., et al. 2024, ApJ, 972, L10
Peeters, E., Habart, E., Berné, O., et al. 2024, A&A, 685, A74
Pereira, R., de Barros, A., Fulvio, D., et al. 2018, MNRAS, 478, 4939
Pontoppidan, K. M., Fraser, H. J., Dartois, E., et al. 2003, A&A, 408, 981
Queiroz, L., Silva, J., Ferrão, L., & Pilling, S. 2025, MNRAS, 537, 3100
Rachid, M. G., Brunken, N., de Boe, D., et al. 2021, A&A, 653, A116
Rachid, M. G., Rocha, W. R. M., & Linnartz, H. 2022, A&A, 665, A89
Riaz, B., Martín, E. L., Bouy, H., & Tata, R. 2009, ApJ, 700, 1541
Rivilla, V. M., Martín-Pintado, J., Jiménez-Serra, I., et al. 2020, ApJ, 899, L28
Rocha, W., McClure, M., Sturm, J., et al. 2025, A&A, 693, A288
Satorre, M. Á., Escribano, B., Santonja, C., et al. 2025, A&A, 703, A89
Schwieterman, E. W., Olson, S. L., Pidhorodetska, D., et al. 2022, ApJ, 937, 109
Sicilia, D., Ioppolo, S., Vindigni, T., Baratta, G. A., & Palumbo, M. E. 2012, A&A, 543, A155
Slavicinska, K., Rachid, M. G., Rocha, W. R. M., et al. 2023, A&A, 677, A13
Smith, Z. L., Dickinson, H. J., Fraser, H. J., et al. 2025, NatAs, 9, 883
Tobin, J. J., Looney, L. W., Li, Z.-Y., et al. 2016, ApJ, 818, 73
Tobin, J. J., Offner, S. S. R., Kratter, K. M., et al. 2022, ApJ, 925, 39
van Gelder, M. L., Ressler, M. E., van Dishoeck, E. F., et al. 2024, A&A, 682, A78
Villanueva, G., Mumma, M., Novak, R., et al. 2013, Icarus, 223, 11
Ziurys, L., Apponi, A., Hollis, J., & Snyder, L. 1994, ApJ, 436, L181

Appendix A: Apertures

The intensity maps at 4.4 μm and selected apertures for the sources described in this Letter are displayed in Fig. A.1. Gaseous CO lines were masked in spectra extracted from the white apertures. Spectra extracted from the green apertures contained clean N_2O features as is. For B1-c a ring aperture was used to avoid gaseous lines towards the center. The data on the sources and the aperture parameters are listed in Table C.1.

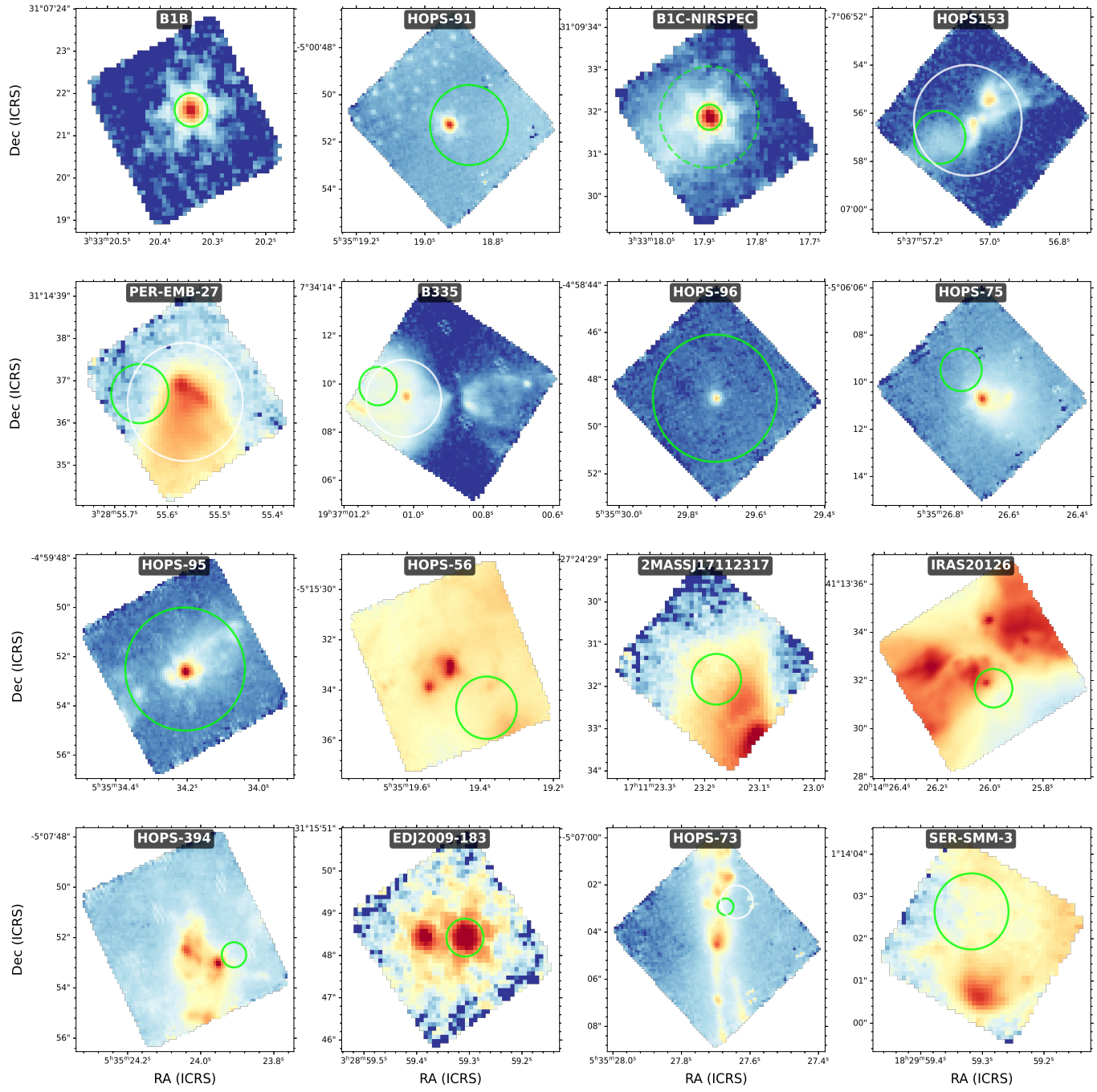

Fig. A.1. Intensity maps at 4.4 μm with the apertures chosen for the fit. Aperture centers and diameters are listed in Table C.1.

Appendix B: Baselines

This section contains original and processed spectra with masked gaseous lines. The anchor points for local continuum subtraction were selected in absorption-free regions to isolate two groups of overlapping features: $^{13}CO_2$, HNCO, N_2O and OCN^-, CO. Most of the points were chosen in the following ranges: 2325–2290 cm^{-1}, between $^{12}CO_2$ and $^{13}CO_2$; 2230–2185 cm^{-1}, between the proposed N_2O and OCN^- feature; 2125–2065 cm^{-1}, next to the CO feature. In a few cases we included additional points outside

these ranges to ensure the conservative estimation of local continuum and peak areas. A polynomial function, with a degree ranging from three to five, was selected to model the continuum. The spectra with the selected continua are shown in Fig. B.1.

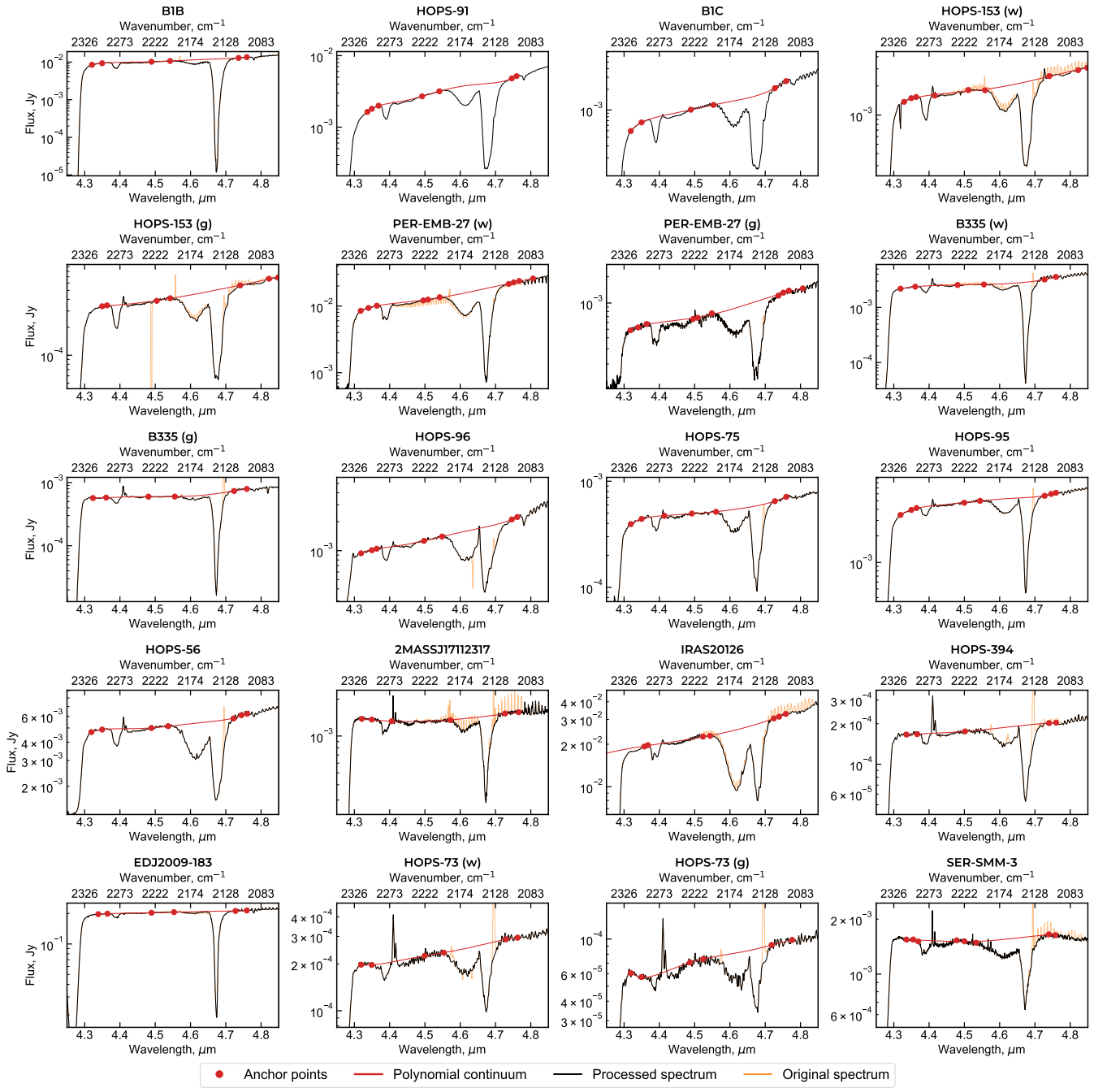

Fig. B.1. Raw and processed observational spectra with fitted polynomial continuum. Anchor points are represented with red dots, fitted continuum with red line. Original and processed observational spectra are shown with orange and black lines, respectively.

Appendix C: Sources and column densities

The sources and apertures' parameters along with the derived column densities are listed in Table C.1. In this work we estimated the column density of $^{13}CO_2$ to be in the range of (1.3 – 11)×10^{16} cm^{-2}. This range is consistent with $^{13}CO_2$ column density range of (1.2 – 8.1)×10^{16} cm^{-2} presented in Brunken et al. (2024), 2.3×10^{16} cm^{-2} value for IRAS 20126 and 2.8×10^{16} cm^{-2} for Per-emb 35 presented in Brunken et al. (2025). Brunken et al. (2024) also presents individual column densities for B1-b, B1-c, EDJ2009-183, SER-SMM-3, PER-EMB-27 are 2.6×10^{16} cm^{-2}, 7.1×10^{16} cm^{-2}, 0.58 – 0.7×10^{16} cm^{-2}, 2×10^{16} cm^{-2} and 5.9×10^{16} cm^{-2}, respectively. These values are lower than ones derived in this work, which is explained by difference in band strengths used.

Column density values for CO obtained in this work are in (64.5 – 464)×10^{16} cm^{-2} range, consistent with, for example, 66×10^{16} cm^{-2} for Ced 110 IRS4B: (Rocha et al. 2025) and (20 – 365)×10^{16} cm^{-2} for Cha I (Smith et al. 2025). Brunken et al.

(2024) also presents individual CO column densities for B1-b, B1-c, EDJ2009-183, SER-SMM-3, PER-EMB-27: 410×10^{16} cm^{-2}, 500×10^{16} cm^{-2}, $(94-100)\times10^{16}$ cm^{-2}, 120×10^{16} cm^{-2} and 340×10^{16} cm^{-2}, respectively. These values are similar with the ones presented in this Letter, given the difference in chosen apertures. Derived OCN^- values are in range of $(0.6-14.6)\times10^{16}$ cm^{-2}, in agreement with 2.6×10^{16} cm^{-2} for IRAS 16253, 5.0×10^{16} cm^{-2} for B335, 6.8×10^{16} cm^{-2} for HOPS 153, 16×10^{16} cm^{-2} for HOPS 370 (Nazari et al. 2024), and 9.2×10^{16} cm^{-2} for Ced 110 IRS4A (Rocha et al. 2025). To the best of our knowledge, there are currently no HNCO estimates in the literature. The band strengths for N_2O at 10 K in various environments were calculated based on 10 K band strength value from Hudson et al. (2017). The values obtained are listed in the Table C.2.

Table C.1. Parameters of the studied objects and quantities derived from the fit.

Source	Class	Coordinates	D	T (K)	Column densities (N), $\times10^{16}$ cm^{-2}					R
			″	N_2O	N_2O	HNCO	$^{13}CO_2$	OCN^-	CO	%
B1-b[a]	0	$3^h33^m20.3415^s$ $31°7'21.6139''$	0.8	12^{+6}_{-2}	1.1±0.1	1.3±0.1	5.0±1.0	4.7±1.0	464±7	0.2
HOPS-91[b]	0	$5^h35^m18.8710^s$ $-5°0'51.2845''$	3.4	23^{+0}_{-1}	0.8±0.2	1.2±0.2	7.0±1.0	10.0±0.8	387±8	0.2
B1-c[a]	0/I	$3^h33^m17.8906^s$ $31°9'31.8779''$	0.6 2.4[g]	23^{+0}_{-4}	2.2±0.2	2.1±0.3	11.0±0.9	13.3±0.7	385±7	0.6
HOPS-153[b] (w)[h]	0	$5^h37^m57.0635^s$ $-7°6'56.2890''$	4.6	18^{+2}_{-2}	1.6±0.3	0.4±0.2	8.3±0.7	10.1±0.6	261±6	0.6
HOPS-153[b] (g)	0	$5^h37^m57.1443^s$ $-7°6'56.9967''$	2.2	12^{+11}_{-2}	1.0±0.2	0.6±0.2	7.9±0.7	11.2±0.6	296±6	0.4
PER-EMB-27[a] (w)	0	$3^h28^m55.5662^s$ $31°14'36.4986''$	2.8	11^{+4}_{-1}	1.3±0.1	1.9±0.1	8.1±0.7	14.6±0.5	295±4	0.4
PER-EMB-27[a] (g)	0	$3^h28^m55.6521^s$ $31°14'36.6958''$	1.4	11^{+2}_{-1}	4.4±0.3	2.9±0.4	8.9±0.5	13.1±0.4	261±4	1.7
B335[c] (w)	0	$19^h37^m1.0285^s$ $7°34'9.4052''$	3.2	23^{+0}_{-1}	1.3±0.1	–	4.0±1.0	4.2±1.0	284±8	0.4
B335[c] (g)	0	$19^h37^m1.1022^s$ $7°34'9.9127''$	1.6	23^{+0}_{-1}	0.7±0.1	–	3.0±1.0	2.4±0.9	236±7	0.3
HOPS-96[b]	0	$5^h35^m29.7202^s$ $-4°58'48.7875''$	5.4	23^{+0}_{-1}	1.6±0.3	0.3±0.1	4.0±1.0	12.6±1.0	212±10	0.8
HOPS-75[b]	0	$5^h35^m26.7402^s$ $-5°6'9.4794''$	1.8	23^{+0}_{-3}	1.2±0.5	0.7±0.5	4.2±0.6	7.8±0.4	193±4	0.6
HOPS-95[b]	0	$5^h35^m34.2059^s$ $-4°59'52.5012''$	5	23^{+0}_{-3}	0.7±0.2	0.2±0.1	4.0±1.0	6.8±0.8	178±6	0.4
HOPS-56[b]	0	$5^h35^m19.3829^s$ $-5°15'34.6982''$	2.48	22^{+1}_{-6}	1.0±0.1	0.6±0.1	4.2±0.4	10.4±0.4	162±3	0.6
2MASSJ17112317[e]	0/I	$17^h11^m23.1784^s$ $-27°24'31.8296''$	1.2	23^{+0}_{-1}	1.2±0.1	–	3.2±0.4	3.5±0.3	124±2	1.0
IRAS20126[d]	0/I	$20^h14^m25.9868^s$ $41°13'31.6776''$	1.6	23^{+0}_{-10}	1.0±0.2	0.3±0.1	3.7±0.4	17.9±0.3	130±2	0.8
HOPS 394[b]	0	$5^h35^m23.9090^s$ $-5°7'52.6847''$	1	20^{+3}_{-10}	1.0±0.4	0.7±0.6	2.5±0.6	5.8±0.6	128±5	0.8
EDJ2009-183[a]	flat	$3^h28^m59.3083^s$ $31°15'48.4229''$	0.9	23^{+0}_{-2}	0.19±0.02	–	1.3±0.3	0.6±0.3	110±2	0.2
HOPS-73[b] (w)	0	$5^h35^m27.6386^s$ $-5°7'2.7197''$	1.4	11^{+12}_{-1}	2.0±0.5	0.8±0.4	3.7±0.6	7.7±0.5	95±4	2.1
HOPS-73[b] (g)	0	$5^h35^m27.6716^s$ $-5°7'2.9227''$	0.7	23^{+0}_{-13}	2.5±0.6	1.2±0.8	2.4±0.7	9.6±0.8	83±6	3.0
SER-SMM-3[f]	0	$18^h29^m59.3176^s$ $1°14'2.6471''$	1.8	23^{+0}_{-1}	0.5±0.4	1.0±0.4	3.0±0.3	7.7±0.3	64±2	0.6

Notes. For each source listed are class, coordinates, diameter of the aperture (D), N_2O temperature, column density for N_2O, HNCO, $^{13}CO_2$, OCN^-, CO and N_2O abundance with respect to CO (R). Protostar classes are taken from: [(a)] Tobin et al. (2016) [(b)] Furlan et al. (2016), Tobin et al. (2022) [(c)] Launhardt et al. (2013) [(d)] Chen et al. (2016) [(e)] Riaz et al. (2009) [(f)] Ortiz-León et al. (2018) [(g)] For B1-c the ring aperture is used, inner and outer diameters are listed. [(h)] W (white) and g (green) indicate the color of the aperture in Fig. A.1.

Table C.2. Absorption band strength values used for the fit.

Molecule	Peak Position (cm^{-1})	Band Strength (cm)	References
N_2O:CO	2235.4	4.9×10^{-17}	this work
N_2O:CO_2	2250	4.7×10^{-17}	this work
N_2O:CO_2:CO	2245.9	5.2×10^{-17}	this work
N_2O:CO_2:N_2	2242.6	6.8×10^{-17}	this work
N_2O:N_2	2234.7	5.8×10^{-17}	this work
HNCO	2255	9.79×10^{-17}	Gerakines et al. (2025)
$^{13}CO_2$	2283	6.8×10^{-17}	Bouilloud et al. (2015)
OCN^-	2170	1.51×10^{-16}	Gerakines et al. (2025)
CO	2139	1.12×10^{-17}	Bouilloud et al. (2015)

Appendix D: Fitting results

The observational spectra for the selected sample of sources, fitted N_2O-bearing laboratory spectra and HNCO Gaussians are shown in Fig. D.1.

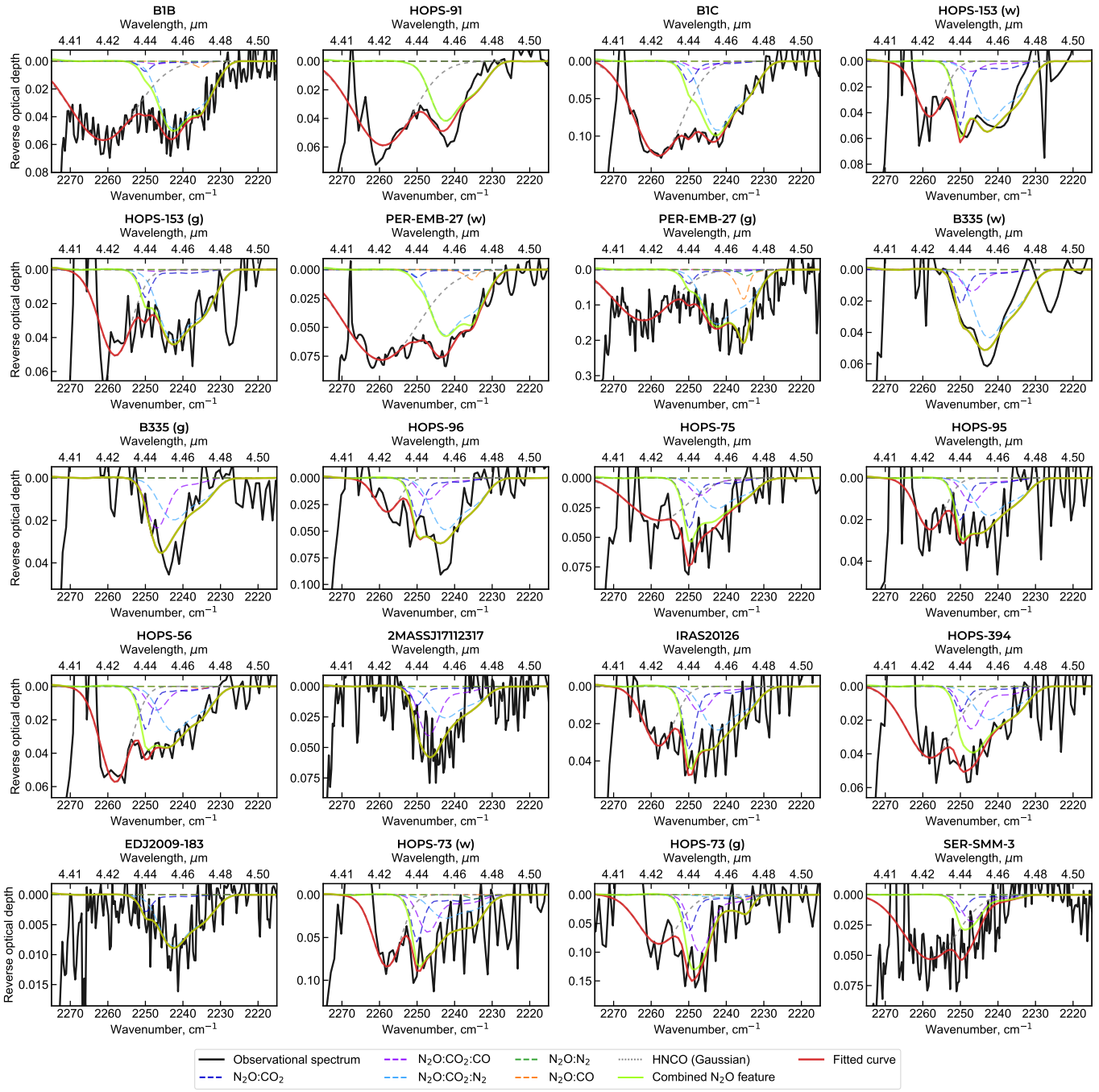

Fig. D.1. Observational data at 4.45 μm, fitted curves and Gaussian function for HNCO. Black line represents the observational spectra, dashed — laboratory spectra of N_2O in apolar environment, short dashed — HNCO Gaussian, green — combined N_2O feature, and red — full fitted curve.